Available online at www.sciencedirect.com
ScienceDirect
Electrochimica Acta 52 (2007) 7061–7067
ELECTROCHIMICA Acta
www.elsevier.com/locate/electacta

Si–carbon core–shell composite anode in lithium secondary batteries

Yoon Seok Jung, Kyu T. Lee, Seung M. Oh *

School of Chemical and Biological Engineering, and Research Center for Energy Conversion & Storage, Seoul National University, Seoul 151-742, Republic of Korea

Received 23 January 2007; received in revised form 12 May 2007; accepted 16 May 2007
Available online 21 May 2007

Abstract

A Si–carbon core–shell powder was prepared via resorcinol-formaldehyde (RF) microemulsion polymerization in the presence of hydrophobized Si nano-particles and subsequent carbonization. The Si nano-particles were completely encapsulated by amorphous carbon shell. With this core–shell approach, the anodic performance of Si electrode for lithium cells has been improved on aspects of Si utilization and cycle retention, which seems to be indebted to the formation of stable electronic conductive network by an intimate contact between Si core and carbon shell. The capacity delivered by this electrode is, however, smaller than that of bare Si due to the presence of RF-derived carbon and electrochemically inactive silicon oxide that was generated during the carbonization process by a reaction between Si and oxygen from the RF gel. The evolution of cracks in the carbon shell after cycling is additional problem to be solved.

Keywords: Li secondary batteries; Silicon; Carbon encapsulation; Nano-particles; Core–shell structure

1. Introduction

Recently, many researches have been devoted to replace the carbon electrode with Li-alloy materials such as Si and Sn for the negative electrode of lithium secondary batteries since the alternatives possess a much higher theoretical capacity ($Li_{15}Si_4$: 3579 mAh g^{-1}, $Li_{22}Sn_5$: 993 mAh g^{-1}) than that of graphite [1–3]. The commercial use of Si electrode is, however, still hindered because it suffers from a rapid electrode degradation. It is generally accepted in the literature that Si electrodes degrade due to the breakdown of conductive network made between Si and carbon particles, which is in turn caused by a severe volume expansion/contraction upon cycling [4–7]. To overcome or alleviate these problems, several approaches have been made with; nano-sized Si powders [8,9], dispersion in inactive [10–13] or active [6,14–20] matrix, amorphous Si powders [4,20], and elastomeric polymer binders [21,22]. Among these, the Si–carbon composites have been attracted much attention since carbon has high electronic conductivity and negligible volume change upon cycling (ca. 10% for graphite) [16–20].

In this work, we have prepared a novel Si–carbon core–shell structure by modifying the resorcinol-formaldehyde (RF) microemulsion polymerization technique [23,24]. The key feature in this preparation is that the Si particles were surface-treated with silylating reagent to impart a hydrophobic character that is necessary for the formation of stable Si–RF sol core–shell structure. After carbonization of the resulting Si–RF gel powder, a Si–carbon core–shell composite was successfully prepared with a uniform carbon coating on Si particles. As will be seen later, however, silicon oxide was generated as a result of reaction between Si and oxygen provided from the RF gel during the carbonization period. The oxide content was precisely determined from the thermogravimetric analysis (TGA) profiles. The electrochemical performance of Si–carbon core–shell electrodes was examined, where a major concern was paid on what effect both the carbon encapsulation and silicon oxide formation has on the capacity and cycle performance of Si–carbon core–shell electrode.

2. Experimental

2.1. Preparation of Si–carbon core–shell powder

The silylation of Si nano-particles was performed according to Scheme 1. In detail, a round-bottom flask containing Si

* Corresponding author. Tel.: +82 2 880 7074; fax: +82 2 872 5755.
E-mail addresses: seungoh@snu.ac.kr, seungoh@plaza.snu.ac.kr (S.M. Oh).

0013-4686/$ – see front matter © 2007 Elsevier Ltd. All rights reserved.
doi:10.1016/j.electacta.2007.05.031

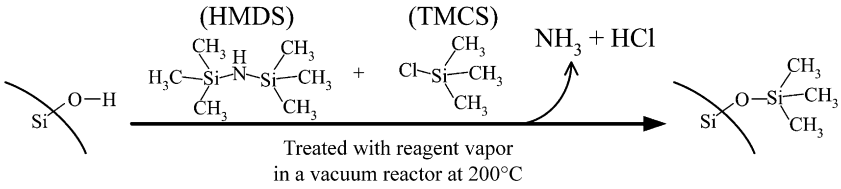

Scheme 1. Silylation procedure for Si nano-particles. The native silanol group was reacted with the silylating reagents.

nano-particles (1.0 g, 30–50 nm, >98%, N & A Materials Inc., USA) was heated in silicon-oil bath to 200 °C under vacuum. After closing the vacuum valve, hexamethyldisilazane (HMDS, 0.8 mL) and chlorotrimethylsilane (TMCS, 0.4 mL) were simultaneously injected. In this process, the native silanol group on Si surface reacts with the silylating reagent. Two reagents were employed to maximize the degree of silylation as suggested in the literature [25,26]. After a reaction for 1 h, the un-reacted reagents and by-products such as NH_3 or HCl were removed by vacuum for 3 h.

For the preparation of core–shell structured Si–RF sol, the silylated Si nano-particles (200 mg) were added into the RF microemulsion, and dispersed by sonication and vigorous stirring. The RF microemulsion was prepared by mixing resorcinol (R, 4 mmol), formaldehyde (F, 4 mol, 300 mL of 37 wt.% aqueous solution), sodium carbonate (0.075 mmol as a catalyst), and cetyltrimethylammonium bromide (CTAB, 1.976 mmol as a surfactant) in de-ionized water (200 mL). For the polymerization of RF sol, the mixture was heated at 85 °C for 3 days, which was followed by drying at the same temperature. The resulting Si–RF gel was heat-treated at 1000 °C for 1 h under argon atmosphere to carbonize the RF gel. In order to address the effect of silicon oxides on the electrochemical performance of Si electrode, a control experiment was made with oxidized Si particles (ox-Si) that were prepared by heat-treatment of bare Si nano-particles (b-Si) at 700 °C for 1 h in air.

2.2. Material characterization

Microscopic investigation was carried out with a JEOL JEM 2000 EXII transmission electron microscope (TEM), a JEOL JEM 3000 F high-resolution transmission electron microscope (HR-TEM), and a JSM 6700F field-emission scanning electron microscope (FE-SEM). For the postmortem TEM analysis, the core–shell Si–carbon electrode after cycling was rinsed with dimethyl carbonate (DMC) in an argon-filled glove box, dried under vacuum, and sonicated to disperse the particles in absolute ethanol. X-ray diffraction (XRD) patterns were recorded using a Bruker D8 Advance with Cu Kα radiation at a scan rate of 1.5° min^{-1}. The elemental analysis was made based on the thermogravimetric analysis (TGA) profiles that were obtained from room temperature to 1350 °C at 20 °C min^{-1} in air with a TA instrument Q 600 simultaneous DSC/TGA analyzer.

2.3. Electrochemical characterization

A beaker-type three-electrode cell was employed to assess the electrochemical performance of samples. The composite electrodes were prepared by spreading a slurry mixture of core–shell powder, Super P (carbon additive for conductivity enhancement) and polytetrafluoroethylene (PTFE, as a binder) (50:20:15, weight ratio) on a piece of copper exmet (as a current collector, apparent area = 1 cm^2). The electrodes were then dried at 120 °C under vacuum for 12 h and subsequently pressed in order to enhance the inter-particle contact and to ensure a better adhesion to the current collector. Lithium foils (Cyprous Co.) were used as the counter and reference electrode, and 1.0 M $LiClO_4$ dissolved in a mixture of ethylene carbonate (EC) and diethyl carbonate (DEC) (1:1, v/v) was used as the electrolyte. The electrochemical performance was examined at a current density of 50 mA g^{-1} in the voltage range of 0.0–2.0 V (versus Li/Li^+). In this report, the lithiation was expressed as discharging, whereas the de-lithiation charging.

3. Results and discussion

3.1. Preparation of Si–carbon core–shell powder

The TEM and HR-TEM images of Si nano-particles are shown in Fig. 1a and b, respectively. The pristine Si powder carries a three-dimensionally agglomerated structure comprising ca. 30–50 nm primary particles (Fig. 1a). As shown in Fig. 1b, the crystalline Si particle is covered with a few nm amorphous SiO_x layer. Because only the particles having sufficiently hydrophobic surface can be encapsulated by RF sol, the surface of Si nano-particles was hydrophobized by silylation [24,25]. The hydrophobic nature can be confirmed by their preference for nonpolar solvents to polar solvents. For instance, the silylated Si nano-particles are readily extracted to *n*-hexane layer from aqueous layer, whereas the un-treated ones remain in aqueous layer.

Once the surface-treated Si nano-particles are added into the RF microemulsion, the Si particles are supposed to place at the innermost region (core) as they are more hydrophobic than RF sol, and the RF sol at the outside (shell). The surfactant micelles likely place at the outermost region to stabilize the Si–RF sol core–shell structure, whereas the catalyst that resides in the aqueous phase now diffuses into the micelles to initiate RF polymerization [23,24]. The core–shell structure can be confirmed by the TEM image shown in the inset of Fig. 1d, where it is seen that the Si–RF gel particle carries a Si particle (darker image) in the core region that is encapsulated by the RF gel layer (lighter image) in the shell. The FE-SEM and TEM images of final Si–carbon core–shell particles are shown in Fig. 1c and 1d, respectively. As seen in Fig. 1c, the carbon coated Si particles also show a three-dimensionally agglomerated structure,

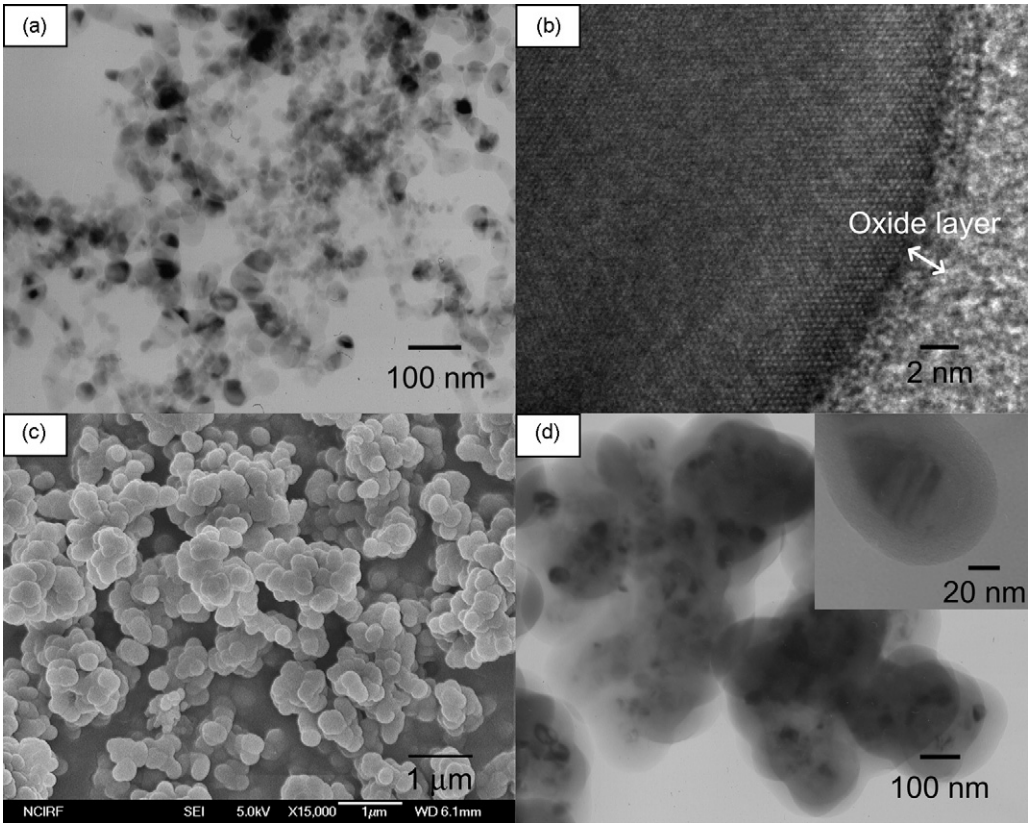

Fig. 1. (a) TEM and (b) HR-TEM images of bare Si nano-particles; (c) FE-SEM and (d) TEM images of Si–carbon core–shell powder. The HR-TEM image of Si–RF gel core–shell powder was presented in the inset of (d).

but the size of primary particles becomes larger, indicative of carbon coating on them. A complete encapsulation of Si nano-particles by carbon layer can be recognized in Fig. 1d, where the darker image again corresponds to Si particles and the lighter one carbon shell layer.

3.2. Elemental analysis based on thermogravimetric analysis profiles

Fig. 2 presents the TGA profiles of bare Si (b-Si), oxidized Si (ox-Si), and Si–carbon core–shell powder (CSP). The b-Si exhibits a noticeable weight increase above 800 °C, which must be due to Si oxidation ($Si + O_2 \rightarrow SiO_2$). The plateau appeared from 1200 °C indicates that the oxidation is completed when the temperature reaches at 1300 °C. The chemical composition of b-Si was calculated using the following relationships:

$$\frac{b_1 + b_2}{a} = \frac{2 \times \text{atomic weight of O}}{\text{atomic weight of Si}} \quad (1)$$

$$\frac{a + b_1 + b_2}{a + b_1} = \frac{W_{1300}}{W_{100}} \quad (2)$$

$$a + b_1 = 100 \quad (3)$$

Here, a and b_1 are the wt.% of Si and oxygen in the samples, respectively, b_2 the weight fraction of oxygen that was incorporated during the TGA experiment up to 1300 °C in air and W_i is the wt.% observed at temperature i (°C) in the TGA profiles. Taking the values of $W_{100} = 99.7$ and $W_{1300} = 204.4$ from the TGA profile (the closed circles), the following result was obtained; $a = 96$, $b_1 = 4$, and $b_2 = 105$ for the bare Si powder. The composition of ox-Si was obtained by the same procedure; $a = 88$, $b_1 = 12$, and $b_2 = 87$ ($W_{100} = 99.9$ and $W_{1300} = 187.1$).

The Si–carbon core–shell powder (CSP) exhibits, after the moisture being removed below 100 °C, a weight loss around 600 °C due to the burn-off of carbon shell and weight increase

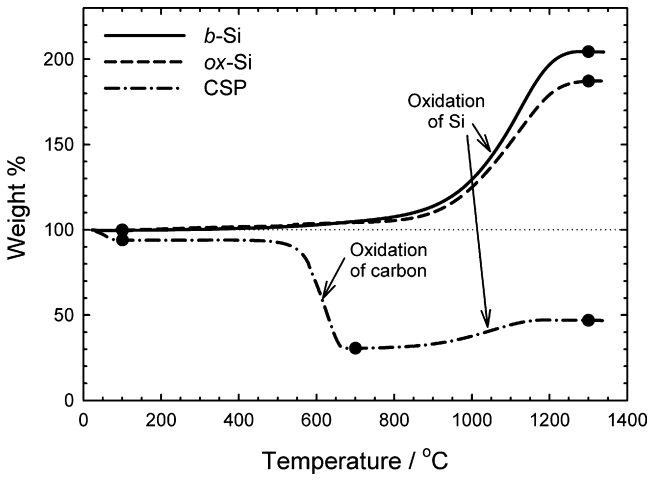

Fig. 2. TGA profiles of bare Si (b-Si), oxidized Si (ox-Si), and Si–carbon core–shell powder (CSP). The heating rate was 20 °C min^{-1} in air. Note that Si oxidation is completed below 1300 °C and carbon oxidation below 700 °C.

Table 1
Chemical composition and electrochemical performance of the samples

Sample	Composition[a] (wt.%)			Charge capacity in the first cycle[b] (mAh g^{-1})	Charge capacity delivered by Si component in the first cycle[d] (mAh g_{Si}^{-1})
	Si	O	C		
b-Si	96	4	–	2350 (2250)[c]	2440
ox-Si	88	12	–	1480 (1380)[c]	1780
CSP	23	8	69	930 (550)[c]	3470

[a] Determined from TGA profiles (Fig. 2). Details are provided in the text.
[b] The arithmetic sum of independent contributions from Si and RF-derived carbon divided by total weight (for instance, Si + SiO_2 + RF-derived carbon for CSP electrode). For the calculation, the specific charge capacity of RF-derived carbon was separately measured to be 400 mAh g^{-1}.
[c] The numbers in parenthesis correspond to the charge capacity delivered by Si component by itself.
[d] The specific charge capacity divided by unit mass of Si.

from 800 °C that is associated with the oxidation of Si core. The chemical composition of CSP was calculated using the following relationships:

$$\frac{b_1 + b_2 + b_3}{a} = \frac{2 \times \text{atomic weight of O}}{\text{atomic weight of Si}} \quad (4)$$

$$\frac{a + b_1 + b_3}{a + b_1 + d} = \frac{W_{700}}{W_{100}} \quad (5)$$

$$\frac{a + b_1 + b_3}{a + b_1} = 1.05 \quad (6)$$

$$\frac{a + b_1 + b_2 + b_3}{a + b_1 + b_3} = \frac{W_{1300}}{W_{700}} \quad (7)$$

$$a + b_1 + d = 100 \quad (8)$$

Here, b_3 is the weight fraction of oxygen that was incorporated by Si oxidation during the TGA experiment below 700 °C and d is the wt. of carbon in the core–shell powder. Two additional assumptions were made for this analysis: the carbon oxidation is completed below 700 °C as seen in Fig. 2 and the weight increase caused by Si oxidation below 700 °C in this sample is 5 wt.%, from which Eq. (6) has been derived. The latter assumption was made based on the TGA profile of b-Si, where the same amount of weight increase (5%) is observed from 100 to 700 °C. Taking the values of $W_{100} = 94.0$, $W_{700} = 30.6$, and $W_{1300} = 46.9$ from the TGA profile, the following result was obtained; $a = 23$, $b_1 = 8$, $d = 69$, $b_2 = 17$ and $b_3 = 2$ for the core–shell powder.

Table 1 summarizes the chemical composition of three samples. It is seen that the b-Si carries 4 wt.% of oxygen as a native oxide, but the oxygen content increases up to 12 wt.% for ox-Si. Unexpectedly, however, the oxygen content in the CSP appears as high as 8 wt.%. The oxygen source should be come from the RF gel that contains oxygen since the carbonization was made under argon atmosphere. Furthermore, it is very likely that SiO_x ($x < 2$) should be converted to SiO_2 by disproportionation reaction ($2SiO \rightarrow Si + SiO_2$) since the carbonization temperature was as high as 1000 °C [27]. But the possibility either for the carbo-thermal reduction ($SiO_2 + C \rightarrow Si + CO_2$) or silicon carbide (SiC) formation is not likely since the carbonization temperature is not high enough [27,28]. The large amount of oxygen in this core–shell powder as an electrochemically inactive and non-conductive SiO_2 must be a disadvantageous feature as the anode for lithium cells. This will be discussed in the next section.

Fig. 3 shows the XRD patterns of b-Si and CSP. All the assignable peaks correspond to those of Si (JCPDS #27-1402), indicative of amorphous nature of silicon oxide and RF-derived carbon. The amorphous SiO_x layer on b-Si has been confirmed on the HR-TEM image (Fig. 1b). The broad peak at 23° in the profile of CSP also indicates that the resulting carbon shell is amorphous. It is known that RF gels are converted to non-crystalline hard carbons upon carbonization [29].

3.3. Electrochemical characterization of Si–carbon core–shell powder

The galvanostatic charge–discharge voltage profiles of CSP electrode are presented in Fig. 4a, where several features are immediately apparent. First of all, the irreversible capacity loss is observed in every cycle. In the first cycle, the irreversible capacity amounts to 800 mAh g^{-1} (1730 mAh g^{-1} for discharging and 930 mAh g^{-1} for charging). Such a large irreversible capacity may arise from several origins [7,8,30]: (i) the solid electrolyte interface (SEI) formation on carbon surface as evidenced by the plateau near 0.9 V in Fig. 4a and (ii) Li^+ ion trapping at void or cavity sites that are populated in the RF-derived hard carbon. Another possible origin is the Li^+ ion trapping in Si matrix, which is commonly observed in Si–carbon composite electrodes [3,7]. That is, Si electrode is swollen due to a vol-

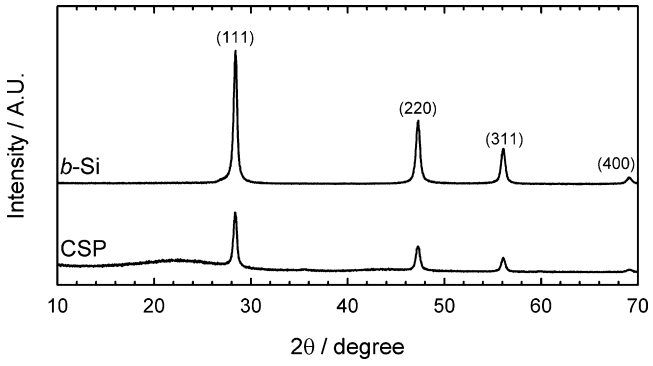

Fig. 3. XRD patterns of bare Si (b-Si) and Si–carbon core–shell powder (CSP). Note that only the diffraction peaks assignable to Si are detected, indicating that both silicon oxide and RF-derived carbon are amorphous.

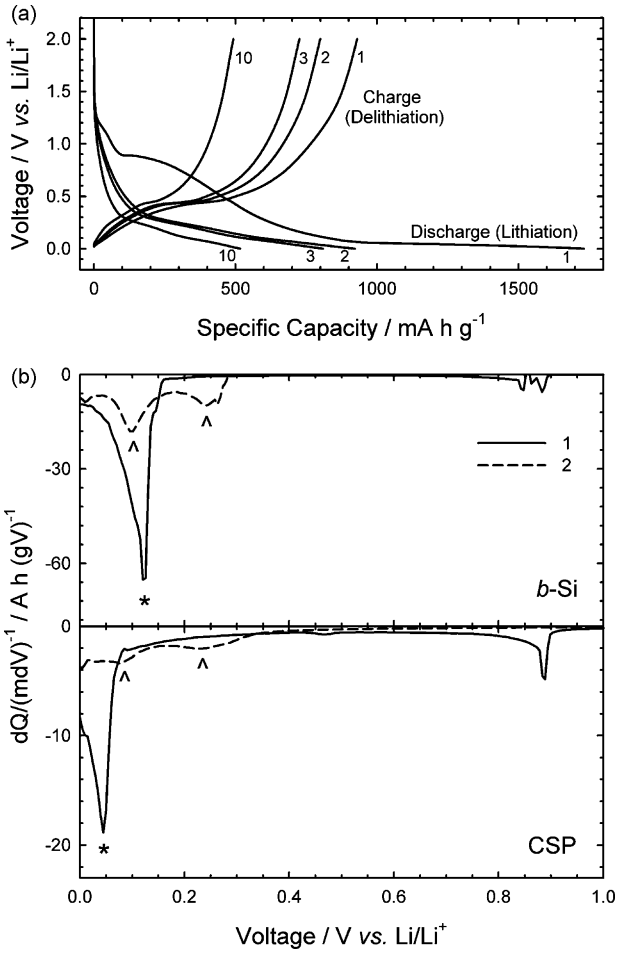

Fig. 4. (a) Charge–discharge voltage profiles of Si–carbon core–shell powders (CSP) cycled between 0.0 and 2.0 V (vs. Li/Li^+) at a rate of 50 mA g^{-1}. The specific capacity was calculated on the basis of total weight ($Si + SiO_2$ + RF-derived carbon). (b) Differential discharging capacity profiles for the first two cycles. Note that the lithiation potential moves to the negative direction with carbon encapsulation.

ume expansion of Si particles in the lithiation period. In the forthcoming de-lithiation period, Si particles are contracted but the electrode layer still remains swollen because it is not elastic. The net result after a cycle is a breakdown of conductive network made between Si and carbon particles, thereby the de-lithiation reaction cannot be completed while Li^+ ions being trapped in Si matrix. In order to see if such an incomplete de-lithiation (Li^+ ion trapping in Si matrix) is indeed occurring in the first cycle, the charging capacity of three electrodes was calculated on the basis of unit mass of Si and listed in the last column in Table 1. In the case of CSP electrode, the value is 3470 mAh g_{Si}^{-1} that is close to the theoretical value (3579 mAh g_{Si}^{-1} as $Li_{15}Si_4$), reflecting that lithiation is completed up to the theoretical value in the first discharging and the concomitant de-lithiation is also almost completed. Note that the complete lithiation in the first cycle is a common feature in both Si thin film and Si–carbon composite electrodes as reported in the literature [3,4,7,12]. The Li^+ ion trapping, however, prevails in both b-Si and ox-Si electrode in the first cycle as listed in Table 1. The charging capacity based on unit mass of Si is 2440 mAh g_{Si}^{-1} for b-Si and 1780 mAh g_{Si}^{-1} for ox-Si electrode, illustrating that the Li^+ trapping is indeed occurring in these electrodes in the first cycle. The lower degree of de-lithiation in these electrodes, after a full lithiation, is a direct result of breakdown in the conductive network that is encountered even after one cycle [7]. The complete de-lithiation observed with CSP electrode can thus be ascribed to the intimate contact made between Si core and carbon shell. It is very likely that the conductive network is still provided by the carbon shell even after a cycle of electrode swelling and contraction, allowing Li^+ ions to be fully extracted.

Another apparent feature in Fig. 4a is that the discharging capacity in each cycle is comparable to the charging capacity in the previous cycle. For instance, the second discharging capacity (922 mAh g^{-1}) is close to the first charging capacity (930 mAh g^{-1}) and the third discharging capacity (809 mAh g^{-1}) to the second charging (800 mAh g^{-1}), manifesting itself that lithiation is possible only to the Li^+ storage sites emptied in the previous de-lithiation step. Also, a steady decrease in discharging capacity with cycling reflects that the empty Li^+ sites become less populated due to a successive accumulation of Li^+ inside Si matrix. The irreversible capacity appeared in CSP electrode from the second cycle is therefore ascribed to the Li^+ trapping in Si matrix. Both SEI formation on carbon surface and Li^+ ion trapping in hard carbons can be discarded since these are known to take place mainly in the first cycle [30].

Fig. 4b displays the differential discharging capacity profiles for b-Si and CSP electrodes. Both electrodes gave one sharp peak (*) below 0.2 V in the first discharging, but two peaks (∧) in the second discharging, indicating that the Si component in the initial sate is crystalline, but becomes amorphous after a cycling [31]. The most revealing feature in Fig. 4b is that the first lithiation reaction in the CSP electrode takes place at ca. 0.07 V lower than that for b-Si as indicated by (*), reflecting that the electrode polarization is larger for the CSP electrode. The sluggish Li^+ diffusion through the carbon shell and SiO_2 layer that may be covered on Si surface seems to be the main reason for the larger polarization. The difference in electrode polarization, however, becomes less significant in the second discharging as indicated by (∧), which may be accounted for by the generation of cracks on both the carbon shell and SiO_2 layer (Fig. 5), which may allow a facilitated Li^+ diffusion into the Si core.

Fig. 6 compares the cycle performance of three electrodes. The CSP electrode delivers a much smaller charge capacity as compared to b-Si, which must be resulted from the presence of RF-derived carbon and electrochemically inactive SiO_2. The smaller capacity of ox-Si electrode must be due to the presence of inactive SiO_2. All the three electrodes suffer from a capacity decay, which must be caused by the successive Li^+ ion trapping in Si matrix as mentioned above. In this work, 23.5 wt.% of conductive carbon (Super P) was loaded, which is somewhat larger than the normal loading, to maintain the conductive network. Even this, the breakdown is seemingly unavoidable.

Even if the CSP electrode is not free from capacity decay, the decay rate is least significant among the three as seen in Fig. 6. This feature seems meaningful if one considers the utiliza-

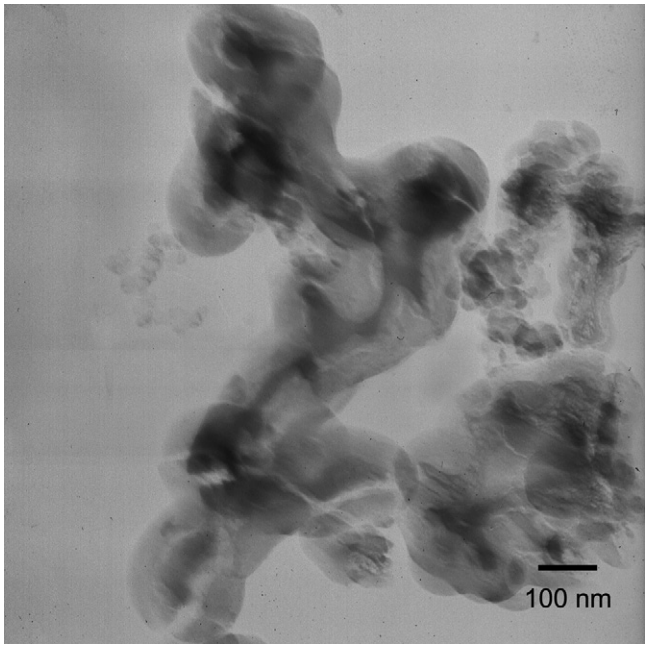

Fig. 5. TEM image of Si–carbon core–shell powder (CSP) taken after 30 cycles. Note the evolution of cracks in the carbon layer.

tion of Si component. As mentioned above, the CSP electrode shows a complete de-lithiation in the first cycle, but the other two electrodes a limited fraction. Even if the extent of lithiation/de-lithiation becomes smaller in the continuing cycle, the utilization of Si is largest for the CSP electrode. Here, the largest Si utilization means the most severe volume change in Si component and thus most serious breakdown of conductive network is being expected. The experimental results, however, indicate that the b-Si and ox-Si electrodes show a poorer cycle retention in spite of limited Si utilization. Along this line, the better cycle performance of CSP electrode can be attributed to the formation of core–shell structure. The Si particles in this structure experience the most severe volume change with the highest degree of lithiation/de-lithiation, but the Li^+ trapping appears least significant. This can be explained by the intimate contact made between Si core and carbon shell even if the breakdown of conductive network is unavoidable due to crack formation and detachment of carbon shell after repeated cycling (Fig. 5).

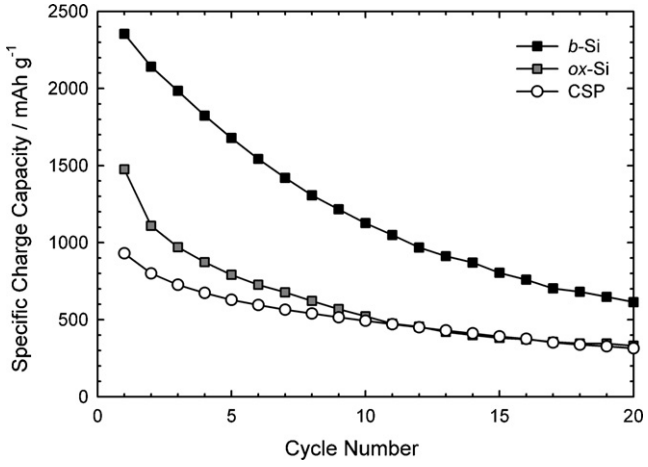

Fig. 6. The specific charge capacity of bare Si (b-Si), oxidized Si (ox-Si), and Si–carbon core–shell powder (CSP) electrodes according to cycle number. The values were calculated on the basis of total weight of electrode material.

One point that should be addressed here is that the non-conductive SiO_2 on Si particles has a negative effect on the anodic performance of Si electrode. Enhanced cycle life by Si–SiO_2 nano-composite that is generated by heat treatment of SiO has been reported [27], where the nano-sized Si particles are dispersed throughout the SiO_2 matrix such that the latter can play a buffering role against the volume change of Si component. In this work, the ox-Si sample that contains 12 wt.% of oxygen exhibits the poorest degree of de-lithiation (1780 mAh g_{Si}^{-1}) in the first cycle (Table 1) but its capacity decay is most significant, which manifests itself that the SiO_2 layer on Si surface can not play the buffering role. Along this line, the oxygen content as SiO_2 should be reduced, for instance, by using oxygen-free polymer precursors. The minimization of RF-derived carbon in CSP is also desirable since the charge capacity of this carbon is much smaller than that of b-Si, and electrolyte decomposition and concomitant SEI formation take place on carbon surface. This may be achieved by decreasing the RF content in the preparation step. These works are undergoing in this laboratory.

4. Conclusion

In this work, a Si–carbon core–shell composite was prepared and its anodic performance in lithium secondary batteries was examined. The following points are summarized.

(i) A stable Si–RF sol core–shell structure was successfully generated by silylating the Si nano-particles, with which a Si–RF gel and eventually Si–carbon core–shell composite was prepared.
(ii) The chemical composition was estimated using thermogravimetric analysis profiles. It was found that electrochemically inactive silicon oxide forms during the carbonization period by a reaction with oxygen contained in the RF gel.
(iii) The Si–carbon core–shell powder delivers an improved anodic performance as compared to the bare Si, which is believed due to the intimate contact made between Si core and carbon shell. Even this, the formation of non-conducting silicon oxide in the carbonization step and crack formation in the course of cycling should be minimized to achieve an enhanced cycle performance.

Acknowledgment

This work was supported by KOSEF through Research Center for Energy Conversion and Storage.

References

[1] M. Winter, J.O. Besenhard, M.E. Spahr, P. Novák, Adv. Mater. 10 (1998) 725.
[2] J.O. Besenhard, J. Yang, M. Winter, J. Power Sources 68 (1997) 87.

[3] M.N. Obrovac, L. Chrstensen, Electrochem. Solid-State Lett. 7 (2004) A93.
[4] T.D. Hatchard, J.R. Dahn, J. Electrochem. Soc. 151 (2004) A838.
[5] U. Kasavajjula, C. Wang, A.J. Appleby, J. Power Sources 163 (2007) 1003.
[6] M. Yoshio, H. Wang, K. Fukuda, T. Umeno, N. Dimov, Z. Ogumi, J. Electrochem. Soc. 149 (2002) A1598.
[7] J.H. Ryu, J.W. Kim, Y.E. Sung, S.M. Oh, Electrochem. Solid-State Lett. 7 (2004) A306.
[8] H. Li, X. Huang, L. Chen, Z. Wu, Y. Liang, Electrochem. Solid-State Lett. 2 (1999) 547.
[9] Z.P. Guo, J.Z. Wang, H.K. Liu, S.X. Dou, J. Power Sources 146 (2005) 448.
[10] I.S. Kim, P.N. Kumta, G.E. Blomgren, Electrochem. Solid-State Lett. 3 (2000) 493.
[11] I.S. Kim, G.E. Blomgren, P.N. Kumta, Electrochem. Solid-State Lett. 6 (2003) A157.
[12] J.W. Kim, J.H. Ryu, K.T. Lee, S.M. Oh, J. Power Sources 147 (2005) 227.
[13] G.X. Wang, L. Sun, D.H. Bradhurst, S. Zhong, S.X. Dou, H.K. Liu, J. Power Sources 88 (2000) 278.
[14] H. Kim, J. Choi, H.J. Sohn, T. Kang, J. Electrochem. Soc. 146 (1999) 4401.
[15] L.Y. Beaulieu, K.C. Hewitt, R.L. Turner, A. Bonakdarpour, A.A. Abdo, L. Christensen, K.W. Eberman, L.J. Krause, J.R. Dahn, J. Electrochem. Soc. 150 (2003) A149.
[16] Y. Liu, K. Hanai, J. Yang, N. Imanishi, A. Hirano, Y. Takeda, Electrochem. Solid-State Lett. 7 (2004) A369.
[17] X. Yang, Z. Wen, X. Zhu, S. Huang, Electrochem. Solid-State Lett. 8 (2005) A481.
[18] G.X. Wang, J.H. Ahn, J. Yao, S. Bewlay, H.K. Liu, Electrochem. Commun. 6 (2004) 689.
[19] T. Hasegawa, S.R. Mukai, Y. Shirato, H. Tamon, Carbon 42 (2004) 2573.
[20] M. Holzapfel, H. Buqa, F. Krumeich, P. Novák, F.M. Petrat, C. Veit, Electrochem. Solid-State Lett. 8 (2005) A516.
[21] J. Li, R.B. Lewis, J.R. Dahn, Electrochem. Solid-State Lett. 10 (2007) A17.
[22] X. Yang, Z. Wen, X. Xu, B. Lin, Z. Lin, J. Electrochem. Soc. 153 (2006) A1341.
[23] K.T. Lee, Y.S. Jung, S.M. Oh, J. Am. Chem. Soc. 125 (2003) 5652.
[24] Y.S. Jung, K.T. Lee, J.H. Ryu, D. Im, S.M. Oh, J. Electrochem. Soc. 152 (2005) A1452.
[25] L.A. Belyakova, A.M. Varvarin, Colloids Surf. A 285 (1999) 285.
[26] H. Buqa, C. Grogger, M.V.S. Alvarez, J.O. Besenhard, M. Winter, J. Power Sources 97 (2001) 126.
[27] T. Morita, N. Takami, J. Electrochem. Soc. 153 (2006) A425.
[28] P. Raveendran, J. Fu, S.L. Wallen, J. Am. Chem. Soc. 125 (2003) 13940.
[29] J.R. Dahn, T. Zheng, Y. Liu, J.S. Xue, Science 270 (1995) 590.
[30] K. Guerin, A. Fevrier-Bouvier, S. Flandrois, B. Simon, P. Biensan, Electrochem. Acta 45 (2000) 1607.
[31] J. Li, J.R. Dahn, J. Electrochem. Soc. 154 (2007) A156.